Photomagnetism in 5 nm nanocrystals of the alkali cation free-CoFe Prussian blue analogue embedded in a silica matrix

Anne Bleuzen, Michel Goncalves, Laura Altenschmidt, Giulia Fornasieri, Amélie Bordage, Eric Rivière

Photomagnetism in 5 nm nanocrystals of the alkali cation free-CoFe Prussian blue analogue embedded in a silica matrix.

Anne Bleuzen*, Michel Goncalves, Laura Altenschmidt, Giulia Fornasieri, Amélie Bordage, Eric Rivière

Email(s): anne.bleuzen@u-psud.fr

Université Paris-Saclay, CNRS, ICMMO, 91405 Orsay cedex, France.

This article has been published with the financial support of BOOK-D 2019

Abstract: 5 nm nanocrystals of CoFe Prussian blue analogue totally exempt from any alkali cation were prepared. Their photomagnetic properties were compared to those of the corresponding powder made of 150 nm particles as well as to those of 5 nm nanocrystals of CoFe PBAs embedded in comparable silica matrices, made of $Co^{II}Fe^{III}$ pairs and prepared under various conditions. The photomagnetic investigation of the nanoparticles exempt of any alkali cation clearly shows that they are transformed by light and the comparison of their photomagnetic properties to those of the powder made of particles of bigger size with the same chemical composition suggests that the species involved in the switching properties are surface species. Furthermore, the comparison of the magnetic properties of nanoparticles prepared under various conditions also suggests that the aggregation state of the nanoparticles in the porous channels of the silica matrix, by modulating inter-particle interactions, plays a predominant role in the magnetic properties of the nanoparticles assemblies.

Keywords: Prussian blue analogue, photomagnetism, electron transfer, nanoparticle, surface effect, superparamagnetism, ordered mesoporous silica monolith, nanocomposite.

I. Introduction

Since their physical properties can be tuned by the application of various external stimuli, switchable molecular materials are promising candidates for the preparation of multifunctional devices [1-7]. Among them, photoswitchable compounds are of particular interest because the associated photo-induced electronic transitions, and therefore the addressing time, are extremely short. Spin-crossover [1] and charge transfer [8] compounds are among the most studied photoswitchable inorganic systems. These compounds are usually obtained in powder or in single-crystal form, so that their integration into real devices necessitates their preparation as nano-objects as well as the knowledge of the effect of size reduction on their properties. Nevertheless, still few works evidence photoswitchable properties in nanoparticles [9-16], and the effect of size reduction on these properties remains an open question.

Several CoFe Prussian blue analogue (PBA) nanoparticles were prepared [14-20] and a photomagnetic effect was evidenced in some of them [14-16]. In this family of compounds, the photomagnetic effect has been widely studied in samples prepared by precipitation in aqueous solution generally made of particles having size ranging from several tens to several hundred nanometers. In such compounds, it has been shown that the photomagnetic effect is due to the photo-induced Co^{III} (Low Spin (LS)) $Fe^{II} \rightarrow Co^{II}$ (High Spin (HS)) Fe^{III} electron transfer in diamagnetic Co^{III}(LS)Fe^{II} pairs [21-24]. It has also been shown that these diamagnetic Co^{III}(LS)Fe^{II} pairs form during the synthesis when alkali cations are inserted within interstitial sites of the well-known face centered cubic (fcc) structure of PBAs and the photomagnetic effect depends on the amount and on the nature of the inserted alkali cations [25,26].

In order to investigate the size reduction effect on the photomagnetic properties of CoFe PBAs, we developed an original strategy based on the use of the nanoporosity of ordered mesoporous silica monoliths as nanoreactor, which allows a precise control of both the size and chemical composition of the particles [27,28]. The growth of the nanoparticles being limited by the silica walls, the diameter of the particles is fixed by the diameter of the pores. In this study, the diameter of the pores and therefore the diameter of the PBA nanoparticles are fixed at 5 ± 0.5 nm. The silica walls are 4 nm thick, so that the distance between two cylindrical pore centers of the silica matrix is 9 nm [27]. Furthermore, as the chemical composition of the reaction medium in the pores can be precisely adjusted, the control of the chemical composition of the nanoparticles should be possible. We started the investigation of size reduction effect on the photo-induced switching phenomenon by studying one of the most well-documented CoFe PBA photomagnetic compound, with the chemical formula $Rb_2Co_4[Fe(CN)_6]_{3.3}\bullet nH_2O$ [25]. Indeed, this compound in powder form combines an important photomagnetic effect and a reproducible synthesis. It is mainly made of $Co^{III}(LS)Fe^{II}$ pairs in its ground state. In the metastable photo-excited state, it mainly contains Co^{II} (HS) Fe^{III} pairs like the alkali cation free CoFe PBA (chemical formula $Co_4[Fe(CN)_6]_{2.7}\bullet nH_2O$), which is very often taken as a model compound for the photo-excited state, and what we also did for the study of the size reduction effect. Thus, by studying 5 nm nanocrystals of the CoFe PBA containing two rubidium cations per unit cell and of the alkali cation free-CoFe PBA (their synthesis is described in reference 29), we recently evidenced a peculiar core-shell structure of their ground states [29]. The contributions of the well-defined core and shell components were extracted from linear combinations of X-ray absorption spectra. The two nanocomposites are named **RbNanoCoFe** and **KNanoCoFe** thereafter. The 'alcali cation free' compound is named **KNanoCoFe** here because it was prepared from the $K_3[Fe(CN)_6]$ metallic salt (it is named **NanoCoFe** in reference 29). If the amount of potassium cation in the final product is so low that potassium can be detected neither by elemental analysis nor by EDX, the compound (and especially the surface of the compound) could be not completely exempt of it. The core-shell structure that was proposed from the X-ray absorption spectroscopy investigation at the transition metal K-edges is schematized in **Figure 1**.

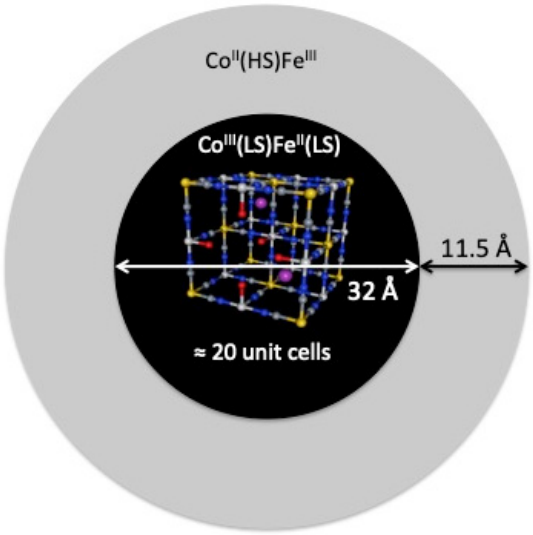

Figure 1. Schematic representation of the core-shell structure of **RbNanoCoFe** and **KNanoCoFe** [29].

The structure of the nanoparticles can be described as follow. They are constituted of a 3 nm spherical core approximately made of 20 unit cells of the well-known face-centered cubic structure of the PBAs, which roughly correspond to 70 CoFe pairs. Whereas these CoFe core pairs are in the $Co^{III}(LS)Fe^{II}$ state in **RbNanoCoFe**, they are in the $Co^{II}(HS)Fe^{III}$ state in **KNanoCoFe**. Whatever the state of the CoFe core pairs, the core is surrounded by a similar shell, the thickness of which corresponds to 2 to 3 metallic layers. This shell, mainly made of $Co^{II}(HS)$ and Fe^{III} species, exhibits a structure different from that of the core [29]. Work is in progress to better characterize it.

RbNanoCoFe exhibits an important photomagnetic effect. The nanocrystals were therefore also studied by X-ray absorption spectroscopy in their photo-excited state. This study shows that after irradiation in the photo-excited state, the spectra of the nanocrystals can no longer be decomposed into two well-defined contributions corresponding to a core and a shell as in the ground state. The nanocrystals rather exhibit one single phase very close to the well-known fcc structure of PBAs mainly made of $Co^{II}(HS)Fe^{III}$ pairs [29]. Thus, the effect of light on the core of the nanocrystals almost corresponds to the well-documented photo-induced $Co^{III}(LS)Fe^{II} \rightarrow Co^{II}(HS)Fe^{III}$ electron transfer, already evidenced in bigger size particles. Unexpectedly, the shell of the nanocrystals also undergoes a significant photo-induced structural change. This photo-induced transformation can be either the consequence of the photo-induced $Co^{III}(LS)Fe^{II} \rightarrow Co^{II}(HS)Fe^{III}$ electron transfer taking place in the core and accompanied by a lengthening of the lattice parameter and therefore of the volume of the core or another photomagnetic effect that has not been described yet. In order to better understand the behaviour of the shell of the nanocrystals under irradiation, one has to study the effect of light on similar shell species in a compound totally exempt from photomagnetic $Co^{III}(LS)Fe^{II}$ pairs. As these photomagnetic $Co^{III}(LS)Fe^{II}$ pairs form in the presence of alkali cations, one solution lies in the preparation of similar nanocrystals totally exempt of alkali cations.
In this work, we report the preparation of nanocrystals totally exempt from any alkali cation and which therefore contain the minimum possible amount of photomagnetic $Co^{III}(LS)Fe^{II}$ pairs, if not any of them. In this way, the core of the nanoparticles is expected to be mainly composed of non-photomagnetic $Co^{II}(HS)Fe^{III}$ pairs surrounded by a shell similar to that of **KNanoCoFe** and **RbNanoCoFe**. The nanocrystals are called **HNanoCoFe** thereafter. They were characterized by X-ray diffraction and infrared spectroscopy and their magnetic properties were compared to those of **KNanoCoFe**. The photomagnetic properties of **HNanoCoFe** were then investigated and compared to those of the corresponding CoFe PBA powder made of 150 nm particles (**HCoFe**). At last, the magnetic properties of **HNanoCoFe** in the photo-excited state are compared to those of 5 nm nanocrystals of CoFe PBAs embedded in comparable silica matrices, made of $Co^{II}Fe^{III}$ pairs and prepared under various conditions.

II. Results and Discussion

The nanocrystals **HNanoCoFe** were prepared within the pores of an ordered mesoporous silica monolith exhibiting a 2D hexagonal organization by adapting a procedure described elsewhere [27]. Briefly, the first PBA precursor (Co(II) cation), added during the synthesis of the silica monolith, is homogeneously distributed as a low-condensed species within the cylindrical and parallel pores after thermal decomposition of the surfactant. The second PBA precursor ($[Fe(CN)_6]^{3-}$ entity) is then introduced in the pores via a simple impregnation step. Thus, the reaction medium can be precisely adjusted. The concentration of Co^{2+} ions is determined by the amount of Co salt added during the synthesis of the monolith and the concentrations of all other species correspond to those of the impregnation solution. In order to prepare nanocrystals completely free of alkali cation, all K^+ cations of the potassium ferricyanide solution were replaced by protons through two salt metathesis reactions described in the experimental part. Ferricyanide is first precipitated as a silver salt, in which no trace of potassium could be detected by EDX. $[Fe(CN)_6]^{3-}$ complexes are redissolved in water by addition of hydrochloric acid, giving an acidic ferricyanide aqueous solution exempt of potassium cations. The ferricyanide concentration of the solution is precisely determined by UV-Vis absorption spectroscopy. Impregnation of the silica monolith by this solution leads to the formation of PBA in the pores of the monolith through a nucleation-growth process in confined space resulting in spherical 5 nm monocrystalline CoFe PBA nanoparticles (TEM images of such nanoparticles have already been presented several times [30], representative images are shown in Figure S1). The X-ray powder diffractogram (Figure S1) of **HNanoCoFe** is very close to that of **KNanoCoFe**, showing that the nanocrystals in both compounds exhibit a very similar crystallographic structure. In a previous work, we investigated by infrared spectroscopy such nanocomposites [29] and we could identify four main cyanide bands, which were assigned as follow: a band at 2166 cm^{-1} assigned to $Co^{II}(HS)$-NC-Fe^{III} core species in a core mainly made of $Co^{II}(HS)$-NC-Fe^{III} pairs, a band at 2130 cm^{-1} assigned to $Co^{III}(LS)$-NC-Fe^{II} core species in a core mainly made of $Co^{III}(HS)$-NC-Fe^{II} pairs, a band at 2190 cm^{-1} assigned to $Co^{II}(HS)$-NC-Fe^{III} shell species, and a band at 2119 cm^{-1} assigned to Fe^{III}-CN terminal species or a minority of $Co^{III}(LS)$-NC-Fe^{II} pairs in a core mainly made of $Co^{II}(HS)NCFe^{III}$ core species. The infrared spectra of **HNanoCoFe** and of **KNanoCoFe** over the energy range corresponding to the stretching vibration of cyanide are shown in Figure 2. Both spectra exhibit the same bands, showing that the nanocrystals contained in both compounds are very close, except that **HNanoCoFe** is completely exempt of alkali cation. The spectra of both compounds, **HNanoCoFe** and of **KNanoCoFe**, exhibit a main band

at 2165 cm^{-1}. This band is assigned to cyanide in the Co^{II}(HS)-NC-Fe^{III} linkages forming the well-known fcc structure of CoFe PBAs [31-37] and contained in the cores of the nanocrystals. The same position of this band in both compounds shows that the core of the nanoparticles are made of exactly the same Co^{II}(HS)-NC-Fe^{III} linkages. Both spectra exhibit a second band of weaker intensity situated at 2125 cm^{-1} and at 2119 cm^{-1} on the spectra of **HNanoCoFe** and **KNanoCoFe** respectively. Given the energy position and the intensity of this band, it can be ascribed either to very small amounts of Co^{III}(LS)-NC-Fe^{II} linkages in the well-known fcc structure of CoFe PBAs, that is to say in the core of the nanocrystals, or to terminal Fe^{III}-CN species belonging to the very last layer at the surface of the nanocrystals. The presence of terminal Fe^{III}-CN species is expected because i) all the $Fe(CN)_6$ entities, are linked by the six N sides of the cyanides to Co cations except those belonging to the last layer at the surface, where Fe^{III}-CN terminal groups can be found, and ii) the nanocrystals were formed in the presence of an excess of $[Fe(CN)_6]^{3-}$ entities. Furthermore, the slight but significant shift of this band from one compound to the other supports the assignment to terminal Fe^{III}-CN species. Indeed, if this band around 2120 cm^{-1} was due to the presence of a small amount of Co^{III}(LS)-NC-Fe^{II} linkages in the core of the nanocrystals mainly made of Co^{II}(HS)-NC-Fe^{III} linkages, the shift of this band from one compound to the other could be explained by different network strains resulting from different Co^{III}(LS)-NC-Fe^{II}/Co^{II}(HS)-NC-Fe^{III} linkages ratio in both compounds. In that case, this presence of Co^{III}(LS)-NC-Fe^{II} linkages would also induce a shift of the band at 2165 cm^{-1} because of the different network strains on the two types of linkages. The fact that the band assigned to the Co^{II}(HS)-NC-Fe^{III} linkages is exactly at the same position in both compounds is rather in favor of the presence of Fe^{III}-CN terminal species. In that case, the shift of the band assigned to terminal Fe^{III}-CN groups can be explained by different interactions between the CN terminal group and K^+ and H^+ cations in the case of **KNanoCoFe** and only H^+ cations in the case of **HNanoCoFe** (due to different synthesis conditions). At last, both spectra exhibit a shoulder of significant intensity and approximately located at 2190 cm^{-1} in **KNanoCoFe** and at 2197 cm^{-1} in **HNanoCoFe**. We proposed in reference 29 to assign this shoulder, present with variable intensity on most of the spectra of CoFe PBAs, to Co^{II}(HS)-NC-Fe^{III} surface species. These species located in the shell of the nanoparticles exhibit a structure different from the Co^{II}(HS)-NC-Fe^{III} linkages contained in the cores. As in the case of the previous band, its slight frequency shift from one compound to the other supports the assignment to surface species.

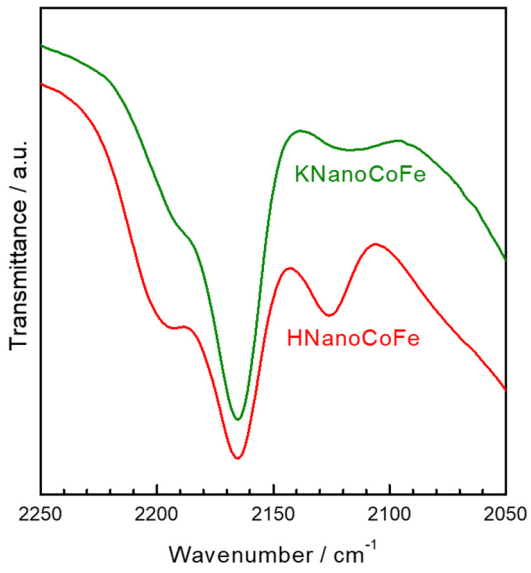

Figure 2. IR spectra of **HNanoCoFe** (red) and **KNanoCoFe** (green).

The magnetic properties of **HNanoCoFe** were first studied before irradiation. The temperature dependence of the zero-field-cooled (ZFC) and field-cooled (FC) magnetization curves of **HNanoCoFe** are shown in Figure 4. They are very close to those already reported for the nanocomposite directly

prepared from the $K_3[Fe(CN)_6]$ salt (**KNanoCoFe**) [28]. The ZFC magnetization curves of **HNanoCoFe** and **KNanoCoFe** exhibit a maximum at very close temperatures (5.4 K for **HNanoCoFe** against 4.6 K for **KNanoCoFe**), which is in agreement with very close chemical compositions, very close structures and very close particles sizes for both compounds. In order to further compare both compounds, Alternating-Current (AC) magnetic susceptibility measurements were performed. AC susceptibility measurements were already performed for **KNanoCoFe**; the whole study reported in reference 28 showed that the nanocrystals contained in **KNanoCoFe** mainly behave as superparamagnets but their magnetic behaviour slightly deviates from pure superparamagnetism. The temperature dependence of the magnetization relaxation time τ was well reproduced with an Arrhenius law (equation 1)

$$\tau = \tau_0 exp\left(\frac{E_a}{k_B T}\right) \quad (1)$$

where τ_0 is the attempt time and its value varies over the 10^{-8} to 10^{-12} s range for pure superparamagnets, k_B is the Boltzmann constant and E_a is the average energy barrier for the spin-flip. In the case of **KNanoCoFe**, the value obtained for τ_0 shows deviation from pure superparamagnetic behaviour, which was explained by three possible reasons: i) weak interparticle interactions, ii) surface effects or iii) presence of $Fe(CN)_6$ vacancies responsible for some kind of frustration and cluster-glass-like behaviour [28]. As the origin of the deviation from pure superparamagnetism is not known, other expressions likely to reproduce the data will not be considered here. The parameters extracted from the AC susceptibility measurements for **HNanoCoFe** (Figure S2a) and the fit of the Arrhenius equation to the temperature dependence of the magnetization relaxation time τ are reported in Table 1, where they are compared to those for **KNanoCoFe**. The τ_0 values are rather comparable for **HNanoCoFe** and **KNanoCoFe**. The amount of alkali cation being extremely small in **KNanoCoFe** (the amount of alkali cations is below the detection threshold for elemental analyses) [38] and zero in **HNanoCoFe**, the chemical composition of the coordination polymer is therefore close to $Co_4[Fe(CN)_6]_{8/3}\square_{4/3}$ (where $\square$ stands for $[Fe(CN)_6]$ vacancies) in both compounds, so that the amount of $Fe(CN)_6$ vacancies can be considered as being the same in both compounds. Therefore, the slightly higher τ_0 value in **HNanoCoFe** can arise from slightly weaker interparticle interactions in **HNanoCoFe** due to different aggregation states of the nanoparticles in the pores or from different surface behaviours. Nevertheless, the behaviour of **HNanoCoFe** is not far from that of **KNanoCoFe** and similar conclusions can be drawn, in agreement with comparable structure, chemical composition and particle size for both compounds.

Table 1. AC magnetic data for **HNanoCoFe**, **HNanoCoFe***, **KNanoCoFe** and **RbNanoCoFe***. The AC magnetic measurements and the fitting of the Arrhenius equation to the experimental data were performed in the same conditions for all compounds. T_{max} is the temperature of the ZFC magnetization maximum and Φ ($(\Delta T_{max}/T_{max})/(\Delta \log f)$ where f is the frequency) is the Mydosh parameter [39].

Sample	T_{max} /K	Φ	Arrhenius	Vogel Fulcher
HNanoCoFe	5.4	0.08	$\tau_0 = (1\pm0.5)\ 10^{-12}$ s $E_a/k_B = 117\pm20$ K	
HNanoCoFe*	5.4	0.07	$\tau_0 = (2\pm0.5)\ 10^{-15}$ s $E_a/k_B = 153\pm20$ K	
KNanoCoFe [28]	4.6	0.07	$\tau_0 = (4\pm0.5)\ 10^{-17}$ s $E_a/k_B = 166\pm20$ K	
RbNanoCoFe* [29]	8.3	0.055	$\tau_0 = (6\pm2)\ 10^{-17}$ s $E_a/k_B = 282\pm50$ K	$\tau_0 = 2\ 10^{-10}$ s $E_a/k_B = 105$ K $T_0 = 3.2$ K

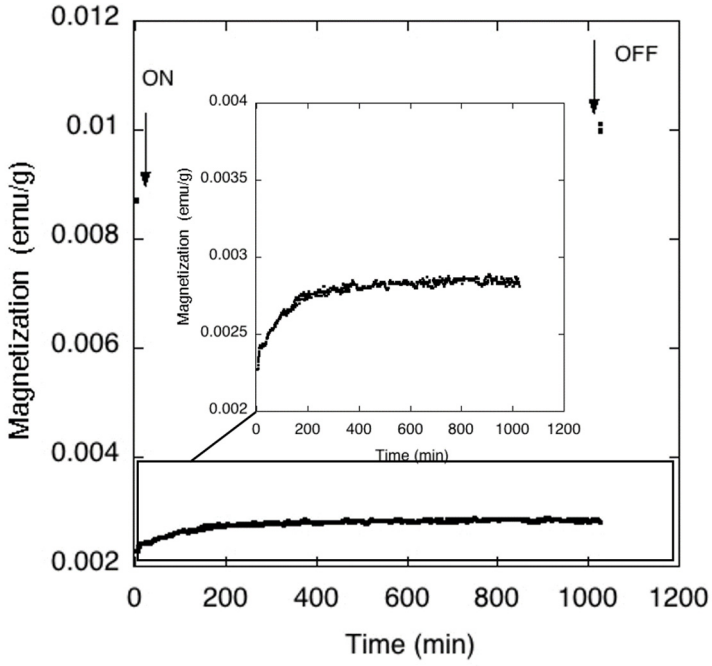

Figure 3. Time dependence of the magnetization of **HNanoCoFe** under irradiation (λ = 635 nm).

The magnetization of **HNanoCoFe** was recorded as a function of time under irradiation in the visible range at 10 K (Figure 3). Under irradiation, the magnetization of **HNanoCoFe** increases slightly but significantly and the magnetization after irradiation once the laser is switched off is clearly higher than before irradiation. Therefore, **HNanoCoFe** exhibits a weak but unquestionable photomagnetic effect. It is worth noticing here that **KNanoCoFe** also exhibits a photomagnetic effect at least comparable to that of **HNanoCoFe** (Figure S3). As the sample was irradiated at 10 K, temperature above the blocking temperature of the nanocrystals, the increase in magnetization cannot be assigned to a reorientation of the magnetic moments of the nanocrystals in the external magnetic field only. The temperature dependence of the magnetization was measured before and after irradiation to check the reversibility of the phenomenon (Figure S4). The two curves being very close to one another, the temperature at which the initial magnetization is fully recovered was determined as the temperature for which the difference of the magnetization after and before irradiation goes to zero (115 K, Figure S4). Unexpectedly, **HNanoCoFe** exhibits an unquestionable and reversible photomagnetic effect. In order to better understand this photomagnetic effect, the magnetic properties of **HNanoCoFe** in the photo-excited state (**HNanoCoFe***) were compared firstly to those of **HNanoCoFe** in the ground state. Secondly, the photomagnetic effect exhibited by **HNanoCoFe** was compared to that of the corresponding powder with the same structure and chemical composition and made of 150 nm particles. At last, the magnetic properties of **HNanoCoFe** in the photo-excited state (**HNanoCoFe***) were compared to those of 5 nm nanocrystals of CoFe PBAs embedded in comparable silica matrices, made of $Co^{II}Fe^{III}$ pairs and prepared in various conditions.

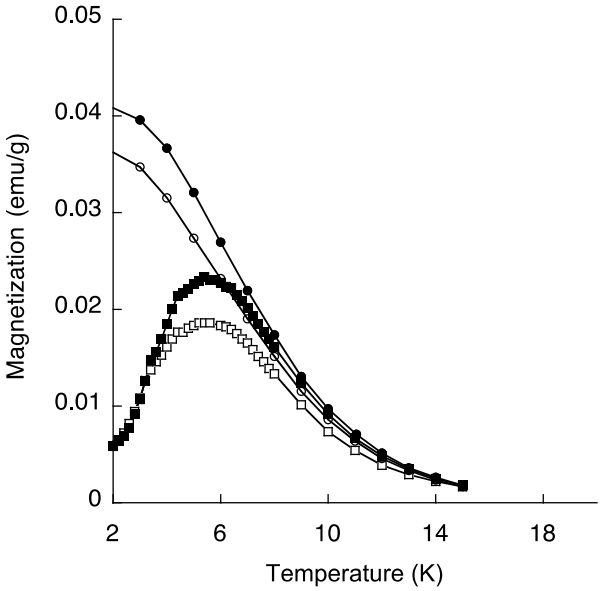

Figure 4. Temperature dependence of the magnetization of **HNanoCoFe** : ZFC before irradiation (white square), ZFC after irradiation (black square), FC before irradiation (white circle) and FC after irradiation (black circle) recorded under an applied field of 50 Oe (λ = 635 nm).

The ZFC/FC magnetization curves of **HNanoCoFe** and **HNanoCoFe*** are shown in Figure 4. The ZFC/FC magnetization curves of **HNanoCoFe*** are different from those of **HNanoCoFe**, which confirms the weak but significant photomagnetic effect exhibited by **HNanoCoFe**. The FC magnetization value at 2 K and the ZFC magnetization maximum value at T_{max} increase by 10% and 20% respectively after irradiation. The temperature of the ZFC magnetization maximum is called T_{max} thereafter. Within the error bar, the T_{max} values determined from the temperature dependence of dM_{ZFC}/dT (Figure S5, Table 1) are the same before and after irradiation for **HNanoCoFe** and **HNanoCoFe***. Irradiation cannot change the aggregation state of the nanoparticles. Therefore, the increase in magnetization reflects an increase of the magnetic moment of each nanocrystal after irradiation, which can have several origins. First, a photo-induced oxidation or reduction of Co or Fe ions by an agent external to the nanocrystals could happen, but it is unlikely since the photomagnetic effect is reversible. Second, even if there is no alkali cation inserted in the nanocrystals, the photo-induced $Co^{III}(LS)Fe^{II} \rightarrow Co^{II}(HS)Fe^{III}$ electron transfer in very few $Co^{III}(LS)Fe^{II}$ diamagnetic pairs cannot be excluded. Indeed, very few $Co^{III}(LS)Fe^{II}$ pairs located in the core of the nanocrystals could be formed due to the random distribution of $Fe(CN)_6$ vacancies. Nevertheless, no IR band clearly assigned to such $Co^{III}(LS)Fe^{II}$ diamagnetic pairs were detected in the infrared spectrum of **HNanoCoFe** (as discussed above) whereas the bands of cyanide species linked to Fe^{II} ions are significantly more intense than those of cyanide species linked to Fe^{III} ones. Third, a photo-induced transformation of the structure of the nanocrystals without electron transfer like the photo-induced structure transformation of the shell of **RbNanoCoFe** detected by X-ray absorption spectroscopy [29] is also possible. In that case, the phenomenon would essentially affect the surface of the nanocrystals. These two last phenomena differ by the location of the involved species: the photo-induced $Co^{III}(LS)Fe^{II} \rightarrow Co^{II}(HS)Fe^{III}$ electron transfer would take place in the core of the nanoparticles, having the well-known fcc structure of PBA (in the ground state, the surface species are mainly made of $Co^{II}(HS)$ and Fe^{III} species with a peculiar structure), while the photo-transformation of the peculiar surface species would take place in the shell of the nanocrystals. In order to identify which of these two phenomena occurs, one has to vary the surface area-to-volume ratio. The higher the surface area-to-volume ratio, the stronger the surface effects are expected to be. CoFe PBA particles completely exempt from alkali cation and having bigger size than the nanocrystals embedded in the silica matrix were also synthesized (see experimental part) and studied. The sample is named **HCoFe** thereafter.

On the SEM images of **HCoFe** (Figure S6), one can see cuboidal particles, the average size of which can be estimated around 150 nm. The infrared spectrum of **HCoFe** (Figure S7) shows the same cyanide bands as the spectrum of **HNanoCoFe** except that i) the relative intensities of the bands are different

and ii) they are slightly shifted due to confinement or size reduction effect. Such a shift is always observed when the IR spectra of nanoparticles embedded in the silica matrix are compared to those of the powder made of particles of bigger size with same chemical composition [27]. Both compounds are therefore made of the same species. The main band at 2160 cm^{-1} is assigned to $Co^{II}(HS)Fe^{III}$ core species. The relative intensities of the bands, which were assigned to surface species on the spectrum of **HNanoCoFe** ($Co^{II}(HS)Fe^{III}$ shell species at 2197 cm^{-1} and Fe^{III}-CN terminal species at 2125 cm^{-1}) are weaker in the powder made of the 150 nm particles, which confirm the assignment of these bands to surface species. The main difference between **HNanoCoFe** and **HCoFe** is therefore the surface area-to-volume ratio. The particles of **HCoFe** were diluted with a silica powder in order to reach the same Co/Si ratio as in **HNanoCoFe** and the ZFC/FC magnetization curves of this sample were recorded before and after irradiation in the same conditions that were used for **HNanoCoFe** (Figure S8). The ZFC/FC magnetization curves of **HCoFe** in the silica powder are nearly the same before and after irradiation. This suggests that the amount of photo-switchable species is much smaller in **HCoFe** than in **HNanoCoFe**. As the surface area to volume ratio of the particles is much smaller in **HCoFe** than in **HNanoCoFe**, this suggests that the photo-switchable species are located at the surface of the particles. An X-ray absorption spectroscopy investigation at the Co and Fe K-edges of **HNanoCoFe** and **HCoFe** is planned in order to clearly identify the photo-switchable species and to study further this peculiar switching phenomenon exhibited by the nanoparticles.

At last, the magnetic properties of **HNanoCoFe*** (photo-excited state) were compared to those of 5 nm nanocrystals of CoFe PBAs embedded in comparable silica matrices, made of $Co^{II}Fe^{III}$ pairs and prepared in various conditions: **HNanoCoFe** (ground state; excess of H^+ and $[Fe(CN)_6]^{3-}$), **KNanoCoFe** (ground state; excess of H^+, $[Fe(CN)_6]^{3-}$ and K^+) [28] and **RbNanoCoFe*** (photo-excited state, excess of H^+, $[Fe(CN)_6]^{3-}$ and K^+; large excess of Rb^+) [29]. The magnetic properties of **RbNanoCoFe** in the ground and the photo-excited states were briefly presented in reference 29. These properties are recalled and further discussed here. The ZFC/FC magnetization curves are shown in Figure S9a. Before irradiation, the ZFC/FC magnetization is low because the core of the nanocrystals is mainly made of $Co^{III}(LS)Fe^{II}$ diamagnetic pairs. The increase in magnetization upon cooling and the irreversibility of the magnetization between the ZFC and FC conditions below 12 K, can be explained by the presence of the peculiar surface contribution mainly made of $Co^{II}(HS)$ and Fe^{III} ions [29]. Contrary to the few $Co^{II}(HS)$ ions (0.7 per unit cell) dispersed in the diamagnetic core, the magnetic moments of the majority $Co^{II}(HS)$ and Fe^{III} surface species can interact and result in the weak but significant collective magnetic behaviour, reflected by the irreversibility between the FC and ZFC magnetization curves. After irradiation, the ZFC magnetization curve of **RbNanoCoFe*** exhibits a maximum at 8.3 K. The irreversibility between the ZFC and FC magnetization curves of **RbNanoCoFe*** up to 20 K suggests the occurrence of inter-particle interactions, which are supported by AC susceptibility measurements for **RbNanoCoFe*** reported in reference 29. Indeed, the AC magnetic data were well fitted by using a Vogel-Fulcher model, which is well suited to take into account inter-particle interactions. All the magnetic data are gathered in Table 1. The magnetic data for **HNanoCoFe***, **HNanoCoFe** and **KNanoCoFe** are also gathered in Table 1. The AC magnetic measurements for **HNanoCoFe*** are shown in Figure S2b. It is striking that the magnetic properties of **HNanoCoFe*** are much closer to those of **HNanoCoFe** and **KNanoCoFe** than to those of **RbNanoCoFe***. The main differences between the magnetic properties of the three first compounds and **RbNanoCoFe*** can be explained in terms of different inter-particle interactions. It is worth recalling here that the particles having the same size as the diameter of the cylindrical pores can aggregate forming chains inside the channels [40], which are separated from each other by 4 nm walls. First, the T_{max} value for **RbNanoCoFe*** (8.3 K) is significantly higher than the T_{max} value for **HNanoCoFe***, **HNanoCoFe** and **KNanoCoFe** (5.4 K, 5.4 K and 4.6 K, respectively) and it is usually assumed that T_{max} shifts to higher temperature with increasing inter-particle interactions [41-44]. Second, the peak of the ZFC magnetization curve, broader for **RbNanoCoFe*** than for **HNanoCoFe** (Figure S10), indicates a broader distribution of energy barriers and relaxation times in **RbNanoCoFe***, assignable to a broader distribution of inter-particle interactions strength [45] (for all compounds the distribution of the particle size is very narrow as it is determined by the diameter of the pores, 5 nm here). Third, the ZFC and FC magnetization curves of **HNanoCoFe***, **HNanoCoFe** and **KNanoCoFe** do not show the same important irreversibility displayed by those of **RbNanoCoFe*** up to 11 K above T_{max}, which is another sign of the broader distribution of energy barriers in **RbNanoCoFe*** due to a broader distribution of inter-particle interactions. Such strengthened inter-particle interactions in **RbNanoCoFe*** have to be related to the aggregation state of the nanocrystals (the nanocrystals can be either well dispersed within the pores or aggregated along the cylindrical pores forming nanocrystals chains).

The presence of an excess of Rb^+ cations in the reaction medium during the formation of the nanocrystals probably favors their aggregation. Given the strong effect of aggregation states on the magnetic properties,

the pure effect of light on the magnetic properties of such nanocomposites can only be evidenced by comparing the magnetic properties of a same sample before and after irradiation. In the case of **HNanoCoFe** this effect is weak but significant and is yet to be fully understood.

III. Conclusions

In a previous work, we evidenced the core shell structure of CoFe Prussian blue analogues and a peculiar behaviour of the surface species in the nanoparticles containing two rubidium cations per unit cell (**RbNanoCoFe**) under irradiation. The photomagnetic study of the nanoparticles exempt of any alkali cation (**HNanoCoFe**) clearly shows that these nanoparticles are significantly transformed by light, which is not the case of the powder made of bigger size particles having exactly the same chemical composition. These results raise completely new questions about size reduction effect on the photomagnetic properties of PBAs and suggest that the species involved in the switching properties could be surface species; work is in progress in order to better understand this phenomenon. Furthermore, the comparison of the magnetic properties of nanoparticles prepared in various conditions also suggests that the aggregation state of the nanoparticles in the porous channels of the silica matrix, by modulating inter-particle interactions, plays a key role in the magnetic properties of these nanoparticles assemblies.

IV. Additional Information

Supporting information is available online. Correspondence and requests for materials should be addressed to corresponding author.

V. Materials and Methods

Sample preparation: Preparation of monoliths with 2D-hexagonal organization containing cobalt(II) ions with a 0.5% Co^{2+}/Si ratio: The synthesis of the monoliths has already been described elsewhere [26]. In a typical procedure, a solution was prepared by mixing 2.4 g of P123 with TMOS (26 mmol, 4 g), as a silica precursor, in a 30 mL polypropylene vial. This solution was stirred in a water bath at 50 °C until the P123 copolymer was dissolved completely and then cooled to room temperature. An aqueous cobalt(II) nitrate acidic solution (69 mM, pH 1.4, 2 mL) was then added to the cooled solution. The mixture was stirred for 2 min and 30 seconds and then divided in four vials, which were sealed and transferred into a thermostated water bath at 23 °C to be aged without stirring for 1 h. The samples were left without caps in the water bath at 23 °C for 1 week to give homogeneous pink glassy silica monoliths containing P123 and Co^{2+} ions. Finally, the P123 copolymer was removed by calcination at 500 °C in air. Precipitation of alkali cation free $Ag_3[Fe(CN)_6]$ salt: A first solution is prepared by dissolving 10 g (30 mmol) of $K_3Fe(CN)_6$ in 200 mL of water. A second aqueous solution is prepared by dissolving 17 g (100 mmol) of $AgNO_3$ in 150 mL of water. The drop-by-drop addition of the silver nitrate solution into the potassium ferricyanide(III) solutions produces an orange precipitate constituted of $Ag_3[Fe(CN)_6]$. The powder is centrifuged, washed five times with deionized water to eliminate all solvated ions, and allowed to dry in air.
Alkali cation free $H_3[Fe(CN)_6]$ aqueous solution 0.6 M: 2.14 g (4 mmol) of $Ag_3[Fe(CN)_6]$ is solubilized in 5 mL aqueous hydrochloric acid solution (1.8 M) and stirred for 4 h. The precipitate constituted by AgCl and residual $Ag_3[Fe(CN)_6]_3$ is separated by filtration. The concentration of $[Fe(CN)_6]^{3-}$ aqueous solution was determined by UV-vis spectroscopy.

HNanoCoFe composite: An impregnating aqueous solution containing $H_3[Fe(CN)_6]$ 0.3 M and HNO_3 0.7 M was prepared. The calcined monoliths containing 0.5% Co^{2+}/Si ions were immersed in heptane (5 mL) and impregnated with a volume of the acidic impregnating solution equal to 80 % of the porous volume. After 1 h, the heptane was removed, and the monoliths were washed five times with water and air-dried. All monoliths were ground before measurements.

HCoFe: Powder **HCoFe** was synthesized by addition of 400 mL of a 6.25×10^{-4} M solution of cobalt(II) nitrate hexahydrate to 50 mL of a 10^{-2} M $H_3[Fe(CN)_6]$ aqueous solution. The addition rate was regulated

to last 3 h. The powders were centrifuged, washed three times with distilled water, and allowed to dry in air.

FTIR Spectroscopy: FTIR spectra were collected in the transmission mode with a PerkinElmer Spectrum 100 spectrometer.

Magnetic and photomagnetic measurements: About 10 mg of powder was spread on a piece of cardboard and some drops of nujol oil were added to fixate it. Direct Current (DC) data were recorded using a XL-7 SQUID magnetometer. Field Cooled-Zero Field Cooled (FC-ZFC) curves were recorded over the 2-15 K temperature range under a 50 Oe magnetic field. Alternative Current (AC) data were recorded using a XL-7 SQUID magnetometer working with an oscillating field of 3 Oe and frequencies ranging from 0.1 to 50 Hz.
For photomagnetic measurements, the sample was irradiated at 10 K in the SQUID with a laser diode (635 nm, 25 mW/cm^2). Samples were irradiated until reaching a photo-stationary state. The temperature dependence of the magnetization was recorded using a XL-7 SQUID magnetometer under a 5000 Oe magnetic field with a sweeping rate of 2 K.min^{-1}.

VI. Conflict of Interests

No conflict of interests.

VII. Acknowledgements

The authors thank the ANR MagDiDi (ANR-17-CE29-0011) for financial support.

VIII. References

1. Gütlich P., Hauser A., Spiering H., *Angew. Chem. Int. Ed.*, **1994**, *33*, 2024–2054.
2. Kahn O., Jay Martinez C., *Science*, **1998**, *279*, 44–48.
3. Létard J.-F., Capes L., Chastanet G., Moliner N., Létard S., Real J.-A., Kahn O., *Chem. Phys. Lett.*, **1999**, *313*, 115–120.
4. Sato O., Einaga Y., Iyoda T., Fujishima A., Hashimoto K., *J. Phys. Chem. B*, **1997**, *101*, 3903.
5. Lepoutre S., Grosso D., Sanchez C., Fornasieri G., Riviere E., Bleuzen A., *Adv. Mater.*, **2010**, *22*, 3992–3996.
6. Molnar G., Cobo S., Real J.A., Carcenac F., Daran E., Vieu C., Bousseksou A., *Adv. Mater.*, **2007**, *19*, 2163–2167.
7. Coronado E., Marti-Gastaldo C., Galán-Mascaros J. R., Cavallini M., *J. Am. Chem. Soc.*, **2010**, *132*, 5456–5468.
8. Sato O., Tao J., Zhang Y.-Z., *Angew. Chem. Int. Ed.*, **2007**, *46*, 2152–2187.
9. Neville S. M., Etrillard C., Asthana S., Létard J.-F., *Eur. J. Inorg. Chem.*, **2010**, *2*, 282–288.
10. Chakraborty P., Boillot M.-L., Tissot A., Hauser A., *Angew. Chem. Int. Ed.*, **2013**, *52*, 7139–7142.
11. Delgado T., Enachescu C., Tissot A., Hauser A., Guénée L., Besnard C., *J. Mater. Chem. C*, **2018**, *6*, 12698–12706.

12. Catala L., Mathonière C., Gloter A., Stéphan O., Gacoin T., Boilot J.-P., Mallah T., *Chem. Commun.*, **2005**, *6*, 746–748.

13. Volatron F., Heurtaux D., Catala L., Mathonière C., Gloter A., Stéphan O., Repetto D., Clemente-Leon M., Coronado E., Mallah T., *Chem. Commun.*, **2011**, *47*, 1985–1987.

14. Moore J. G., Lochner E. J., Ramsey C., Dalal N. S., Stiegman A. E., *Angew. Chem. Int. Ed.*, **2003**, *42*, 2741–2743.

15. Pajerowski D. M., Frye F. A., Talham D. R., Meisel M. W., *New J. Phys.*, **2007**, *9*, 222–233.

16. Fornasieri G., Bleuzen A., *Angew. Chem. Int. Ed.*, **2008**, *47*, 7750–7752.

17. Vo V., Van Minh N., Lee H. I., Kim J. M., Kim Y., Kim S., *Mater. Res. Bull.*, **2009**, *44*, 78–81.

18. Mouawia R., Larionova J., Guari Y., Oh S., Cook P., Prouzet E., *New J. Chem.*, **2009**, *33*, 2449–2456.

19. Durand P., Fornasieri G., Baumier C., Beaunier P., Durand D., Riviere E., Bleuzen A., *J. Mater. Chem.*, **2010**, *20*, 9348–9354.

20. Lartigue L., Oh S., Prouzet E., Guari Y., Larionova J., *Mater. Chem. Phys.*, **2012**, *132*, 438–445.

21. Sato O., Iyoda T., Fujishima A., Hashimoto K., *Science*, **1996**, *272*, 704–705.

22. Yokoyama T., Ohta T., Sato O., Hashimoto K., *Phys. Rev. B*, **1999**, *58*, 8257–8266.

23. Yokoyama T., Kigushi M., Ohta T., Sato O., Einaga Y., Hashimoto K., *Phys. Rev. B*, **1999**, *60*, 9340–9346.

24. Cartier dit Moulin C., Villain F., Bleuzen A., Arrio M.-A., Sainctavit P., Lomenech C., Escax V., Baudelet F., Dartyge E., Gallet J.-J., Verdaguer M., *J. Am. Chem. Soc.*, **2000**, *122*, 6653–6658.

25. Bleuzen A., Lomenech C., Escax V., Villain F., Varret F., Cartier dit Moulin C., Verdaguer M., *J. Am. Chem. Soc.*, **2000**, *122*, 6648–6652.

26. Cafun J.-D., Champion G., Arrio M.-A., Cartier dit Moulin C., Bleuzen A., *J. Am. Chem. Soc.*, **2010**, *132*, 11552–11559.

27. Delahaye E., Moulin R., Aouadi M., Trannoy V., Beaunier P., Fornasieri G., Bleuzen A., *Chem. Eur. J.*, **2015**, *21*, 16906–16916.

28. Moulin R., Delahaye E., Bordage A., Fonda E., Baltaze J.-P., Beaunier P., Rivière E., Fornasieri G., Bleuzen A., *Eur. J. Inorg. Chem.*, **2017**, *10*, 1303–1313.

29. Bordage A., Moulin R., Fonda E., Fornasieri G., Rivière E., Bleuzen A., *J. Am. Chem. Soc.*, **2018**, *140*, 10332–10343.

30. Fornasieri G., Aouadi M., Durand P., Beaunier P., Rivière E., Bleuzen A., *Chem. Commun.*, **2010**, *46*, 8061–8063.

31. Sato O., Einaga Y., Iyoda T., Fujishima A., Hashimoto K., *J. Phys. Chem. B*, **1997**, *101*, 3903–3905.

32. Sato O., Einaga Y., Fujishima A., Hashimoto K., *Inorg. Chem.*, **1999**, *38*, 4405–4412.

33. Shimamoto N., Ohkoshi S.-I., Sato O., Hashimoto K., *Inorg. Chem.*, **2002**, *41*, 678–684.

34. Lezna R.O., Romagnoli R., de Tacconi N. R., Rajeshwar K., *J. Phys. Chem. B*, **2002**, *106*, 3612–3621.

35. Nakamoto K., *Infrared and Raman Spectra of Inorganic and Coordination Compounds*, John Wiley & Sons, Inc. Hoboken, New Jersey, **2008**.

36. Reguera E., Bertran J. F., Diaz C., Blanco J., Rondon S., *Hyperfine Interact.*, **1990**, *53*, 391–395.

37. Lejeune J., Brubach J.-B., Roy P., Bleuzen A., *C. R. Chimie*, **2014**, *17*, 534–540.

38. Aouadi M., Fornasieri G., Briois V., Durand P., Bleuzen A., *Chem. Eur. J.*, **2012**, *18*, 2617–2623.

39. Mydosh J. *A. in Spin Glasses*, Taylor and Francis, Washington, DC, **1993**.

40. Moulin R., Fornasieri G., Impéror-Clerc M., Rivière E., Beaunier P., Bleuzen A., *ChemNanoMat*, **2017**, *3*, 833–840.

41. Zhang X.X., Wen G.H., Xiao G., Sun S., *J. Magn. Magn. Mater.*, **2003**, *261*, 21–28.

42. Mikhaylova M., Kim D.K., Bobrysheva N., Osmolowsky M., Semenov V., Tsakalakos T., Muhammed M., *Langmuir*, **2004**, *20*, 2472–2477.

43. Poddar A., Bhowmik R.N., De A., Sen P., *J. Magn. Magn. Mater.*, **2009**, *321*, 2015–2020.

44. Gonzalez M., Martin-Fabiani I., Baselga J., Pozuelo *J., Mater. Chem. Phys.*, **2012**, *132*, 618–624.

45. Tadic M., Kusigerski V., Markovic D., Milosevic I., Spasojevic V., *J. Magn. Magn. Mater.*, **2009**, *321*, 12–16.

Received: 16 December 2019
Accepted: 05 March 2020
Published online: 20 March 2020

ORCID ID for authors
Anne Bleuzen: 0000-0001-9885-4378
Giulia Fornasieri: 0000-0001-7115-9666
Amélie Bordage: 0000-0001-6452-547X
Eric Rivière: 0000-0003-1261-3149